

Implementation of Real Gas Effects in the Wind-US Flow Solver*

Dennis Lankford,[†] Stan Powell,[‡] and Terry Hand

Aerospace Testing Alliance, Arnold Engineering Development Center, Arnold AFB, TN 37389

Abstract

The Wind-US flow solver has been modified to include real gas thermodynamic properties and real gas fluxes of conserved variables. The real gas evaluations relevant to a specific molecule have been isolated to a single subroutine so that any substances can be implemented relatively easily. Molecular nitrogen and hydrogen have been implemented in the program to date. The real gas model has been implemented in the Wind-US Roe approximate Riemann solver at this time. The real gas nitrogen model has been used to predict converging-diverging nozzle flow at total pressures ranging from nominally 250 to 20,000 psi at a nominal stagnation temperature of 3000°R and exit Mach numbers of 8 to 14. A comparison of the 20,000-psi results with data is presented in this paper. The real gas hydrogen model is used to model high-pressure shock tube calculations relevant to analysis of light gas hypervelocity gun range facilities.

I. Introduction

Hypersonic flight and testing result in flows where physical gas dynamic phenomena occur that are neglected in ideal gas models. These phenomena include chemical reaction, ionization, thermal nonequilibrium, and intermolecular forces. While all these phenomena could be considered real gas effects, with regard to this paper, real gas effects are defined as the effects caused by high density as explained by John D. Anderson, Jr.¹. This is the definition adopted by the Test Medium Working Group of the Scramjet Test Standards Working Group of the JANNAF Air Breathing Panel.

The impetus for the extension of the Wind-US² code for real gas flows was the need to establish a capability to analyze hypervelocity flow facilities at AEDC. Two facilities of particular interest are the Hypervelocity Wind Tunnel 9 Facility and the Hypervelocity Gun Range Facility.

Tunnel 9 is a blowdown facility with a nozzle set designed for operational Mach numbers of 7, 8, 10, 14, and 16.5 at simulated critical altitude regimes. At Mach 14 and 16.5, Reynolds numbers of 3.8×10^6 and 3.24×10^6 , respectively, can be attained. This facility utilizes nitrogen as the working gas with supply pressures up to 1900 atmospheres and supply temperatures up to 3650°R. These facility supply conditions result in real gas flows in the subsonic portion of the converging-diverging nozzles.

Impact and lethality testing are accomplished at AEDC in the Hypervelocity Gun Range facilities. These facilities employ a two-stage light gas gun to drive projectiles to hypervelocity. As part of an ongoing development, an existing two-stage light gas launcher was modified to a free piston shock tunnel configuration. This facility uses an explosive-driven free piston to drive a shock in an impulse tunnel that will provide capabilities for studying hypersonic real-gas aerodynamic and combustion/propulsion effects at very high Mach number conditions. As part of an ongoing facility development program, a goal of a 100-kpsi supply pressure has been set. Modeling this high-pressure system requires a real gas equation of state (EOS) for the molecular hydrogen driver gas.

* The research reported herein was performed by the Arnold Engineering Development Center (AEDC), Air Force Materiel Command. Work and analysis for this research were performed by personnel of Aerospace Testing Alliance, the operations, maintenance, information management, and support contractor for AEDC. Further reproduction is authorized to satisfy needs of the U. S. Government.

[†] Senior Member, AIAA.

[‡] Associate Fellow, AIAA.

Most modern shock-capturing techniques for the solution of the compressible Euler or Navier Stokes equations do some form of flux splitting that requires an evaluation of the eigenvalues and eigenvectors for the system of equations in conservation form. The procedure for obtaining the equations that are ultimately solved by Wind-US is to write the Navier-Stokes equations in conservative form in Cartesian coordinates. The flux derivatives are then transformed from Cartesian coordinates to computational space. The conservation equations are linearized in terms of the flux Jacobians with respect to the conserved variables. Eigenvalues and eigenvectors of these flux Jacobians are needed to diagonalize the flux terms. The procedure for obtaining these matrices is well established for ideal gases,^{3,4} and the procedure for real gases is similar, with differences between real gas and ideal gas being confined to three parameters (see details below).

II. Evaluation of Real Gas Thermodynamic Properties

Since the difference between the ideal gas and real gas formulations depends on the EOS, the form of the EOS that was used is discussed first. Other authors^{5,6} have previously implemented real gas EOS in the solution of the Navier-Stokes equations. Choi, Oh, and Jeung include a discussion of a general form for the thermodynamic relations governing a real gas but appear only to have implemented the Van der Waals EOS in published results. Li, Xia, and Merkle use a general EOS, but they use a table look-up from the REFPROP database,⁷ which seems awkward. For the implementations in Wind-US, curve fits were used as discussed below.

The thermally perfect EOS, $p = \rho R_u T/M$ (where p is the absolute pressure, ρ is the mass density, R_u is the universal gas constant, T is the absolute temperature, and M is the molecular weight), is adequate to describe the fluid in most aerodynamic flows. In some cases (typically, hypersonic simulation facilities), the density is sufficiently high that the thermally perfect EOS is no longer accurate. At high densities intermolecular distances are reduced enough for intermolecular forces to become significant, and higher order equations of state such as van der Waals, Redlich-Kwong, or other virial equations are required.⁸ The EOS takes many forms, but all are empirical, based on measurements rather than on some deeper understanding of the behavior of fluids at high density. Since they are based on experimental measurements, their range of applicability is limited by the range of the experimental data. Different forms of the equations display different characteristics when extrapolated, but all EOS will produce implausible results if extrapolated far enough. Span⁹ is recommended for a complete discussion of the topic. The specific heat and related thermodynamic properties are also modified and are taken to be a function of both density and temperature, e.g., $c_p = c_p(\rho, T)$, in contrast to the more ordinary ideal gas assumption in which these properties are a function of temperature alone.

The real gas subroutines incorporated in Wind-US evaluate the enthalpy, speed of sound, and entropy as functions of density and temperature. Since the curve fits are written with density and temperature as independent variables, iterative methods are used to return properties in terms of any other two variable combinations of pressure, temperature, and density. The enthalpy, internal energy, and isentropic speed of sound are computed in the real gas routine. An effective gamma is computed as the speed of sound squared and divided by RT to allow the real gas speed of sound to be retrieved as needed elsewhere in the code, including the eigenvalues of the flux Jacobians. As shown in the next section, the Roe fluxes are computed with the speed of sound, enthalpy, and derivatives of pressure evaluated using real gas relationships. The real gas pressure is obtained elsewhere in the code from $p = (\beta - 1)\rho e$, which correctly returns pressure since β is h/e . The real gas subroutine also returns the following derivatives: $\partial p / \partial T|_{\rho}$, $\partial p / \partial \rho|_T$, $\partial h / \partial \rho|_T$, $\partial s / \partial \rho|_T$, $\partial e / \partial T|_{\rho}$, $\partial h / \partial T|_{\rho}$ and $\partial p / \partial \rho|_s$.

A. Nitrogen Equation of State

The thermodynamic properties of N_2 were calculated using the EOS formulated by Reynolds.¹⁰ The equation, $P = P(\rho, T)$ is a power series in density, through ρ^9 , plus a power series in density, through ρ^{13} , divided by an exponential of density squared. The coefficients of the power series are polynomials in temperature. A total of 33 constants are used to represent the high-density contribution to the pressure. The limiting form of the equation is the thermally perfect EOS as density decreases. Pressure can be calculated directly, given temperature and density. An iterative procedure is used to calculate density (or temperature) if pressure and temperature (or density) is known. Analytic derivatives are used in Newton iteration, and the convergence is rapid.

The thermally perfect, isochoric specific heat, c_{v0} , was calculated from the equation given in Ref. 10. The form and the constants used in c_{v0} are independent of the high density EOS for an equation of the form used here.

The high-density contributions to other thermodynamic properties are calculated by evaluation of appropriate integrals of the proper derivatives of the EOS. For simplicity, all of the calculations are performed in a single subroutine. The accuracy of the EOS and the subroutine used to implement it were checked by comparing the property values with the comparable numbers from the NIST Webbook.⁷

In order to examine the possible consequences of the thermodynamics models, authors calculated a one-dimensional expansion to compare the difference between ideal gas, thermally perfect but calorically imperfect, and real gas assumptions. The total conditions for the expansion were at a pressure of 77 MPa (11,236 psia) and a temperature of 842°K (1055°F). The real gas compressibility factor, $z = pM/pRT$, was 1.32 at the total conditions. The compressibility factor at the sonic point was 1.17 and was 1 ± 0.01 in the freestream. The speed as a function of area ratio is shown in Fig. 1 below. It can be seen that there is little difference between the ideal gas ($\gamma = 1.4$) assumption and the thermally perfect assumption. The similarity is a result of the relatively low temperature. However, the real gas speed is substantially higher than that of the other models, roughly 20 percent higher at the sonic point and 5 percent higher at an area ratio of 100. Thus the necessity of including real gas effects is established for these total conditions and for higher total pressures with similar temperatures.

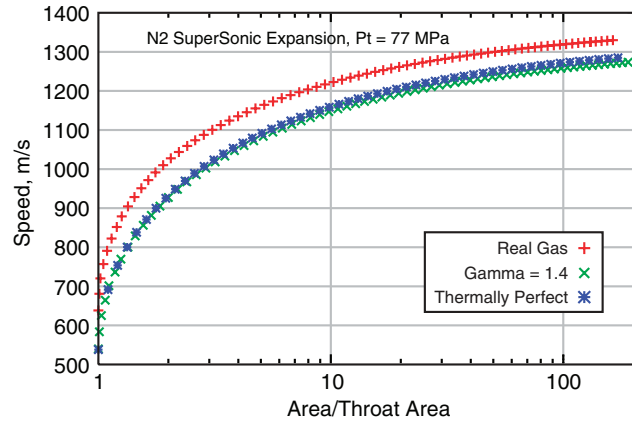


Figure 1. Comparison of Thermodynamic Models for High-Pressure Expansions

B. Hydrogen Equation of State

The literature, including Ref. 10, contains many examples of EOS for hydrogen in the high-density regime. However, none of the equations located covered the range required for the problem at hand; thus an extrapolation of the EOS is required.

Since no applicable data were found, direct comparisons of predictions and data cannot be performed to assess accuracy. Rather, direct comparisons were done where data were available, and the plausibility of the extrapolated values was checked over the whole range. This was a “sanity” check only and dependent largely upon engineering judgment, but it is the best available. The specific heat, c_{v0} , was calculated from equations appropriate to the low-density limit over the temperature range required.

III. Real Gas Roe Approximate Riemann Solver

Wind-US solves the conservation form of the Navier-Stokes equations in curvilinear coordinates with total energy being the conserved variable in the energy equation. The auxiliary equations relating pressure, enthalpy, and internal energy to density and temperature depend on the gas model being used, where the available gas models are either ideal, perfect, or real. For an ideal gas, specific heat at constant pressure and specific heat at constant volume are constants. The perfect gas model includes single species or multi-species mixtures that are thermally perfect and calorically imperfect. In this case, the enthalpy for each species is a function of temperature only. For a real gas, the EOS is generally given by a polynomial in density and temperature, and the enthalpy is a function of two independent thermodynamic properties. The real gas thermodynamic curves described above evaluate expressions in powers of density and temperature. However, for the purpose of deriving the solution algorithm, it is simpler to consider enthalpy as a function of pressure and density because the two are dependent variables in the nonconservative form of the Navier-Stokes equations.

Following a procedure similar to that of ideal gas to obtain the real gas algorithm, the conservative Wind-US form of the Navier-Stokes equations is written in Cartesian coordinates as:

$$\frac{\partial Q}{\partial t} + \nabla \cdot (\vec{F} - \vec{F}_v) = S, \text{ where } Q = \begin{bmatrix} \rho \\ \rho \vec{u} \\ \rho e \\ \rho_i \end{bmatrix} \text{ and } \vec{F} = \begin{bmatrix} \rho \vec{u}^T \\ \rho \vec{u} \vec{u}^T + pI \\ (\rho e + p) \vec{u}^T \\ \rho_i \vec{u}^T \end{bmatrix} \quad (1)$$

where \vec{u} is velocity, e is total specific energy, ρ_i is species i density, and \vec{F}_v is the viscous flux vector. At present, only single-component real gases are being considered; therefore, the fourth element of the Q and \vec{F} vectors are eliminated. In addition, the source vector S is zero. The linearized version of the resulting equation can be expressed as follows:

$$\frac{\partial Q}{\partial t} + (\vec{A} + \vec{A}_v) \cdot \nabla Q = 0, \text{ where } \vec{A} = \frac{\partial \vec{F}}{\partial Q} \text{ and } \vec{A}_v \text{ is the viscous flux Jacobian.} \quad (2)$$

Equation (1) is then transformed to computational coordinates to obtain the following:

$$\frac{\partial \hat{Q}}{\partial t} + \hat{\nabla} \cdot (\vec{\hat{F}} - \vec{\hat{F}}_v) = 0, \text{ where } \hat{Q} = \frac{1}{J} Q \text{ and } \vec{\hat{F}} = \begin{bmatrix} \frac{1}{J} (\nabla_\xi \cdot \vec{F}) \\ \frac{1}{J} (\nabla_\eta \cdot \vec{F}) \\ \frac{1}{J} (\nabla_\zeta \cdot \vec{F}) \end{bmatrix} \quad (3)$$

Here, J is the Jacobian of the transformation, $\hat{\nabla}$ is the del operator in the transformed coordinates and ξ , η , and ζ are the computational coordinates. After linearizing and noting that J cancels out, we see that this equation can be written as:

$$\frac{\partial Q}{\partial t} + (\vec{\bar{A}} + \vec{\bar{A}}_v) \cdot \hat{\nabla} Q = 0, \text{ where } \vec{\bar{A}} = \begin{bmatrix} \nabla_\xi \cdot \vec{A} \\ \nabla_\eta \cdot \vec{A} \\ \nabla_\zeta \cdot \vec{A} \end{bmatrix} \quad (4)$$

The three flux Jacobian matrices, corresponding to the three coordinate directions that are represented by $\vec{\bar{A}}$ are not evaluated directly, but are obtained from the nonconservative flux Jacobians via the same process that has been used to develop the ideal gas flux Jacobians. The x-component of the $\vec{\bar{A}}$ matrix (with y and z-components being similar in form) for an arbitrary gas is given by:

$$A_x = \frac{\partial F_x}{\partial Q} = \begin{bmatrix} 0 & 1 & 0 & 0 & 0 \\ -u^2 + p_{,\rho} & 2u + p_{,\rho u} & p_{,\rho v} & p_{,\rho w} & p_{,Et} \\ -uv & v & u & 0 & 0 \\ -uw & w & 0 & u & 0 \\ u(p_{,\rho} - H) & H + p_{,\rho u} u & p_{,\rho v} u & p_{,\rho w} u & (p_{,Et} + 1)u \end{bmatrix} \quad (5)$$

where $H = h + (1/2)V^2$, $V = \sqrt{u^2 + v^2 + w^2}$, Et is total energy, and h is static enthalpy. Throughout this paper, a subscript with a comma indicates a partial derivative with respect to the subscript variable.

The nonconservative form of the Navier-Stokes equations can be written in linearized form as:

$$\frac{\partial q}{\partial t} + (\vec{\hat{a}} + \vec{\hat{a}}_v) \cdot \hat{\nabla} q = 0, \text{ where } \vec{\hat{a}} = \begin{bmatrix} \nabla \xi \cdot \vec{a} \\ \nabla \eta \cdot \vec{a} \\ \nabla \zeta \cdot \vec{a} \end{bmatrix} \quad (6)$$

Here, \vec{a} is the nonconservative flux Jacobian, and the nonconservative vector of dependent variables is given by:

$$q = [\rho \quad \bar{u} \quad p]^T \quad (7)$$

Equation (6) can be obtained from the conservative equation, Eq. (4), by replacing Q with $P^{-1}q$ and multiplying on the left by P to obtain

$$I \frac{\partial q}{\partial t} + P \vec{\hat{A}} P^{-1} \hat{\nabla} q + P \vec{\hat{A}}_v P^{-1} \hat{\nabla} q = 0 \quad (8)$$

where P^{-1} is the Jacobian matrix $\partial Q / \partial q$

Only the inviscid flux Jacobian, the second term of Eq. (6), is considered for the remainder of this section, since it is needed to obtain the inviscid Roe flux vector. As has been done for ideal gas, the eigenvectors and eigenvalues are obtained for the nonconservative flux Jacobian, and since the nonconservative and conservative matrices are related by a similarity transformation, these values are the same for both. The differences between ideal gas and real gas occur in the evaluation of the matrix P , the matrix P^{-1} , and the thermodynamic properties. In the development of these matrices, it is not necessary to distinguish between ideal gas and real gas if a general expression for enthalpy and the EOS are used. At this point, the enthalpy is chosen as a function of two thermodynamic variables. Pressure and density are a natural choice since they are contained in the nonconservative dependent variable vector and result in the following relations:

$$h = h(p, \rho), \quad p = p(\rho, T), \quad e = e(p, \rho), \quad Et = \rho e + 1/2 \rho V^2 = \rho h - p + 1/2 \rho V^2 \quad (9)$$

where $V = \text{sqrt}(u^2 + v^2 + w^2)$

With these relationships defined, the derivatives needed to determine the P and P^{-1} matrices can be derived. For convenience, groupings of terms in these matrices containing enthalpy and enthalpy derivatives are defined as follows:

$$\varphi = h + \rho h_{,\rho}, \quad \beta = (\rho h_{,p} - 1)^{-1}, \quad \text{and } \alpha = V^2 / 2 \quad (10)$$

These groupings of terms occur only in the last row of the transformation matrix and isolate the difference between real and ideal gas (note that β in this section is not the same as the β defined in the previous section).

$$P = \begin{vmatrix} 1 & 0 & 0 & 0 & 0 \\ -u\rho^{-1} & \rho^{-1} & 0 & 0 & 0 \\ -v\rho^{-1} & 0 & \rho^{-1} & 0 & 0 \\ -w\rho^{-1} & 0 & 0 & \rho^{-1} & 0 \\ \beta(\alpha - \varphi) & -\beta u & -\beta v & -\beta w & \beta \end{vmatrix} \quad P^{-1} = \begin{vmatrix} 1 & 0 & 0 & 0 & 0 \\ u & \rho & 0 & 0 & 0 \\ v & 0 & \rho & 0 & 0 \\ w & 0 & 0 & \rho & 0 \\ \alpha + \varphi & \rho u & \rho v & \rho w & \beta^{-1} \end{vmatrix} \quad (11)$$

The nonconservative flux Jacobian is obtained by a single matrix multiplication for each direction by using the following relationship:

$$\vec{\hat{a}} = P \frac{\partial \vec{F}}{\partial q} \text{ to obtain } \hat{a}_k = \begin{vmatrix} U & \rho k_{,x} & \rho k_{,y} & \rho k_{,z} & 0 \\ 0 & U & 0 & 0 & \rho^{-1} k_{,x} \\ 0 & 0 & U & 0 & \rho^{-1} k_{,y} \\ 0 & 0 & 0 & U & \rho^{-1} k_{,z} \\ 0 & \rho c^2 k_{,x} & \rho c^2 k_{,y} & \rho c^2 k_{,z} & U \end{vmatrix} \quad (12)$$

where $U = k_{,x}u + k_{,y}v + k_{,z}w$, c is the characteristic speed and k is replaced by ξ , η , or ζ for the fluxes in the three grid coordinate directions. The \hat{a}_k matrices can be obtained from the corresponding eigenvalue and eigenvector matrices as

$$\hat{a}_k = T_k \Lambda_k T_k^{-1} \quad (13)$$

where the eigenvalues of the \hat{a}_k matrices are similar in form to the ideal gas and are given by:

$$\Lambda_k = \begin{vmatrix} U & 0 & 0 & 0 & 0 \\ 0 & U & 0 & 0 & 0 \\ 0 & 0 & U & 0 & 0 \\ 0 & 0 & 0 & U + \bar{c} & 0 \\ 0 & 0 & 0 & 0 & U - \bar{c} \end{vmatrix} \quad (14)$$

$$\text{where } \bar{c} = c \sqrt{k_{,x}^2 + k_{,y}^2 + k_{,z}^2}$$

The corresponding Eigenvectors are also similar to the ideal gas form of the equations, as shown below.

$$T_k = \begin{vmatrix} -\tilde{k}_{,x} & \tilde{k}_{,y} & \tilde{k}_{,z} & \frac{\rho}{c\sqrt{2}} & \frac{\rho}{c\sqrt{2}} \\ 0 & -\tilde{k}_{,z} & \tilde{k}_{,y} & \frac{\tilde{k}_{,x}}{\sqrt{2}} & -\frac{\tilde{k}_{,x}}{\sqrt{2}} \\ \tilde{k}_{,z} & 0 & -\tilde{k}_{,x} & \frac{\tilde{k}_{,y}}{\sqrt{2}} & -\frac{\tilde{k}_{,y}}{\sqrt{2}} \\ -\tilde{k}_{,y} & \tilde{k}_{,x} & 0 & \frac{\tilde{k}_{,z}}{\sqrt{2}} & -\frac{\tilde{k}_{,z}}{\sqrt{2}} \\ 0 & 0 & 0 & \frac{\rho c}{\sqrt{2}} & -\frac{\rho c}{\sqrt{2}} \end{vmatrix} \quad T_k^{-1} = \begin{vmatrix} \tilde{k}_{,x} & 0 & \tilde{k}_{,z} & -\tilde{k}_{,y} & \frac{\tilde{k}_{,x}}{c^2} \\ \tilde{k}_{,y} & -\tilde{k}_{,z} & 0 & \tilde{k}_{,x} & -\frac{\tilde{k}_{,y}}{c^2} \\ \tilde{k}_{,z} & \tilde{k}_{,y} & -\tilde{k}_{,x} & 0 & -\frac{\tilde{k}_{,z}}{c^2} \\ 0 & \frac{\tilde{k}_{,x}}{\sqrt{2}} & \frac{\tilde{k}_{,y}}{\sqrt{2}} & \frac{\tilde{k}_{,z}}{\sqrt{2}} & \frac{1}{\rho c \sqrt{2}} \\ 0 & -\frac{\tilde{k}_{,x}}{\sqrt{2}} & \frac{\tilde{k}_{,y}}{\sqrt{2}} & \frac{\tilde{k}_{,z}}{\sqrt{2}} & -\frac{1}{\rho c \sqrt{2}} \end{vmatrix} \quad (15)$$

The characteristic speed of sound for a general gas obeying the thermodynamic functional form specified above is given by

$$c^2 = \beta(h - \varphi) \quad (16)$$

$$\text{or, using Eq. (10), } c^2 = -\beta \rho h_{,\rho} = \rho h_{,\rho} (1 - \rho h_{,p})^{-1}$$

At this point, the distinction between real and ideal gas can be made. For an ideal gas

$$\beta = \gamma - 1, \quad \varphi = h - c_p T, \quad \text{and} \quad c^2 = \gamma R T \quad (17)$$

While, for the real gas relations above,

$$\beta = \frac{\left. \frac{\partial p}{\partial T} \right|_{\rho}}{\rho c_v}, \quad \varphi = h + \rho \left. \frac{\partial h}{\partial \rho} \right|_T - \frac{\rho c_v \left. \frac{\partial p}{\partial \rho} \right|_T}{\left. \frac{\partial p}{\partial T} \right|_{\rho}} - \left. \frac{\partial p}{\partial \rho} \right|_T \quad \text{and} \quad c^2 = - \frac{\left. \frac{\partial p}{\partial T} \right|_{\rho}}{\rho c_v} \left[\rho \left. \frac{\partial h}{\partial \rho} \right|_T - \frac{\rho c_v \left. \frac{\partial p}{\partial \rho} \right|_T}{\left. \frac{\partial p}{\partial T} \right|_{\rho}} - \left. \frac{\partial p}{\partial \rho} \right|_T \right] \quad (18)$$

The conservative flux Jacobian matrix can now be obtained in terms of the above eigenvalues, and eigenvectors and the dependent variable transformation matrices as

$$\hat{A}_k = P_k^{-1} \hat{a}_k P_k = P_k^{-1} T_k |\Lambda_k| T_k^{-1} P_k \quad (19)$$

Roe's numerical flux function can now be written as:

$$\tilde{F}_{1/2} = \frac{1}{2} [F(Q_R) + F(Q_L) - |\delta F|] \quad (20)$$

where $|\delta F| = P_k^{-1} T_k |\Lambda_k| T_k^{-1} P \delta Q$

IV. Pitot Pressure and Total Conditions

Iterative methods are required to compute the total conditions and the pitot pressure when the real gas EOS is used. To compute the supersonic pitot pressure, one first calculates flow across a normal shock, and the total conditions are computed after the shock. The equations governing a normal shock are given by

$$\rho_2 u_2 = \rho_1 u_1, \quad Mom = p_2 + \rho_2 u_2^2 = p_1 + \rho_1 u_1^2, \quad H_t = h_2 + \frac{1}{2} u_2^2 = h_1 + \frac{1}{2} u_1^2 \quad \text{and} \quad \rho = \rho(p, h) \quad (21)$$

where the subscripts 1, 2, and 3 (below) indicate the regions before the shock, after the shock, and at the pitot tube, respectively. All the conditions in front of the shock are known or can be computed from static conditions. The total enthalpy, momentum, and mass flux across the shock are constant, and the entropy must increase. One performs the iteration for conditions behind the shock by computing initial guesses for the conditions behind the shock using ideal gas relations. The difference in total enthalpy and momentum before and after the shock is computed and iterated on until the differences are less than an acceptable limit and are given by

$$\Delta H_t^n = H_t - (h_2 + 0.5u_2^2)^n, \quad \Delta Mom^n = Mom - (p_2 + \rho_2 u_2^2)^n \quad (22)$$

These quantities after the shock are taken as a function of temperature and density; therefore, the total differentials are given by

$$dH_t = \left. \frac{\partial H_t}{\partial T} \right|_{\rho} dT + \left. \frac{\partial H_t}{\partial \rho} \right|_T d\rho \quad \text{and} \quad dMom = \left. \frac{\partial Mom}{\partial T} \right|_{\rho} dT + \left. \frac{\partial Mom}{\partial \rho} \right|_T d\rho \quad (23)$$

These equations are solved simultaneously for dT and $d\rho$ using Eq. (21) relationships to obtain.

$$dT_2^n = \left[\left(\frac{\partial h_2}{\partial \rho_2} - \frac{(\rho_1 u_1)^2}{\rho_2^3} \right) \Delta Mom - \left(\frac{\partial p_2}{\partial \rho_2} - \frac{(\rho_1 u_1)^2}{2\rho_2^2} \right) \Delta H_t \right]^n \frac{1}{\det^n}$$

and

$$d\rho_2^n = \left[\left(\frac{\partial p_2}{\partial T_2} \right) \Delta H_t - \left(c_v + \frac{\left(\frac{\partial p_2}{\partial T_2} \right)}{\rho_2} \right) \Delta Mom \right]^n \frac{1}{\det^n}$$

where

$$\det^n = \left\{ \left[\frac{\partial h_2}{\partial \rho_2} - \frac{(\rho_1 u_1)^2}{\rho_2^3} \right] \frac{\partial p_2}{\partial T_2} - \left[\frac{\partial p_2}{\partial \rho_2} - \frac{(\rho_1 u_1)^2}{2\rho_2^2} \right] \left[c_v + \frac{\frac{\partial p_2}{\partial T_2}}{\rho_2} \right] \right\}^n \quad (24)$$

At this point the properties downstream of the shock are reevaluated by computing:

$$T_2^{n+1} = T_2^n + dT_2^n, \quad \rho_2^{n+1} = \rho_2^n + d\rho_2^n, \quad \text{and} \quad u_2^{n+1} = \rho_1 u_1 / \rho_2^{n+1} \quad (25)$$

The real gas subroutine is then called to recalculate static pressure and enthalpy after the shock plus the required derivatives above. The procedure continues until the total enthalpy change and momentum change are small enough.

The pitot pressure is obtained by computing the total pressure behind the shock. Finding the total pressure and total temperature from post-shock static conditions for the real gas is also an iterative process similar to the shock solution. In this case, since the entropy and total enthalpy are constant behind the shock, the total differential of enthalpy and entropy are used as follows:

$$dH_t = \left. \frac{\partial H_t}{\partial T} \right|_{\rho} dT + \left. \frac{\partial H_t}{\partial \rho} \right|_T d\rho \quad \text{and} \quad dS_t = \left. \frac{\partial S_t}{\partial T} \right|_{\rho} dT + \left. \frac{\partial S_t}{\partial \rho} \right|_T d\rho \quad (26)$$

with $\Delta H_t = H_t - h_3$ and $\Delta S_t = s_2 - s_3$

Simultaneous solution of these equations is given by

$$dT_3^n = \left[\left(\frac{-R}{\rho_3} \right) \Delta H_t - \left(\frac{\partial h_3}{\partial \rho_3} \right) \Delta S_t \right]^n \frac{1}{\det^n}, \quad d\rho_3^n = \left[\left(\frac{-c_v}{T_3} \right) \Delta H_t - \left(c_v + \frac{\frac{\partial p_3}{\partial T_3}}{\rho_3} \right) \Delta S_t \right]^n \frac{1}{\det^n} \quad (27)$$

$$\text{and } \det^n = \left[\left(c_v + \frac{\frac{\partial p_3}{\partial T_3}}{\rho_3} \right) \left(\frac{-R}{\rho_3} \right) - \frac{c_v}{T_3} \frac{\partial h_3}{\partial \rho_3} \right]^n$$

Once the iterative procedure reduces the total enthalpy and entropy changes to acceptable magnitudes, the total temperature is the current iterated value, and the total pressure is obtained from the real gas subroutine with temperature and density known.

V. Boundary Conditions

Characteristic boundary conditions use the eigenvalues and eigenvectors derived above. Therefore, the form appropriate to the assumed gas model for β , φ , and c , as defined in Eq. (16), should be used for the boundary conditions incorporated in the solver. The compatibility equations can be obtained by multiplying Eq. (4) (not including the viscous flux) by the matrix containing the eigenvectors as rows. Letting $E_R = T_k^{-1} P_k$ represent this matrix,

$$E_R \frac{\partial Q}{\partial t} + E_R \bar{A}_v \cdot \hat{\nabla} Q = 0 \quad (28)$$

For a specific eigenvalue, Λ_i as represented in Eq. (14), the compatibility equation can be obtained from Eq. (28) as (see Janus⁴ for details):

$$E_{Ri} \frac{\partial Q}{\partial t} + \Lambda_i E_{Ri} \hat{\nabla} Q = 0 \quad \text{or at a boundary} \quad \frac{\partial W_i}{\partial t} + \Lambda_i \hat{\nabla} W_i = \frac{dW_i}{dt} = 0 \quad (30)$$

where $W_i = E_{Ri} Q$ is the i^{th} characteristic variable.

For each eigenvalue representing a wave traveling from the interior flow toward the boundary, Eq. (30) is used as a boundary condition, while physical boundary conditions are used for eigenvalues going in from the boundary toward the interior. Specifically, for subsonic total inflow conditions, the $U - \bar{c}$ characteristic variable is set using Eq. (30) while the procedure using Eqs. (26) and (27) is used to establish the static conditions at the inflow from specified total pressure and temperature.

VI. Real Gas Computations

A. Mach 14 Nozzle

The real gas Wind model was used to compute the high total pressure, i.e., high Reynolds number conditions, in the AEDC Tunnel 9 nozzle. The nozzle consisted of a 7-in.-long converging section followed by a 479-in.-long contoured diverging section; a 36-in.-long tangent cone extension was added for comparison with data taken in the test cell 24 in. downstream of the nozzle exit. The inlet diameter was 3.986 in., the throat diameter was 0.99 in., the diameter at the end of the first computational zone was 3.986 in., and the exit diameter was 60.74 in. A two-dimensional axisymmetric grid was used, and three turbulence models were investigated: the k-epsilon, SST, and Spalart-Allmaras (S-A). The Spalart-Allmaras model yielded the best overall results. The real gas model was used to simulate test conditions for a Mach 14 case with a total pressure of 19,980 psi and a total temperature of 3303°R. The results of this computation are shown in Figs. 2 through 9. Figure 2 shows the overall geometry of the converging-diverging nozzle and contour plots of Mach number for the perfect gas model (top) versus the real gas model (bottom). The magnitude of the expansion can be ascertained from the size of the small subsonic section compared to the final cross-sectional area and the nominal exit Mach number of 14. The range of the Mach contours is limited for improved clarity. In comparing the perfect gas versus the real gas exit Mach numbers, authors found that whereas the perfect gas attained a Mach

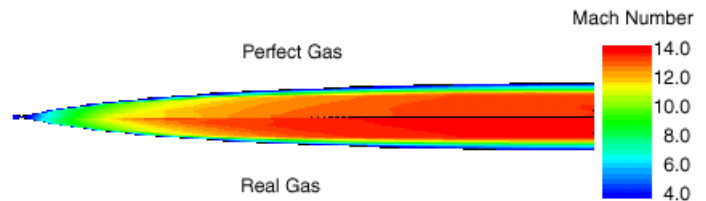


Figure 2. Comparison of Mach Number for Perfect and Real Gas Models

number of 13.377, the real gas attained a Mach number of 13.927. It will be shown that most of the differences between the two cases were originated in the subsonic and far upstream portion of the diverging nozzle.

Figures 3 and 4 show the first computational zone, which contains the converging portion of the nozzle and the initial part of the diverging nozzle. Since the total inlet pressure and temperature were prescribed, there was very little difference between the inlet static values.

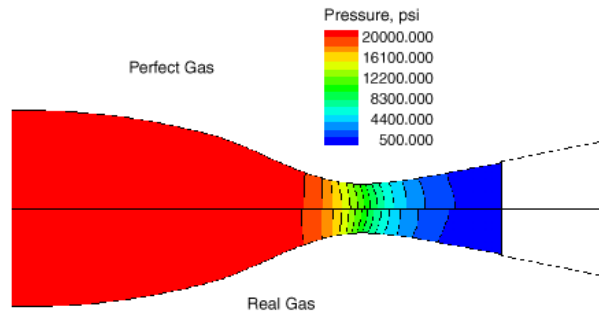


Figure 3. Comparison of Pressure for Perfect and Real Gas Models

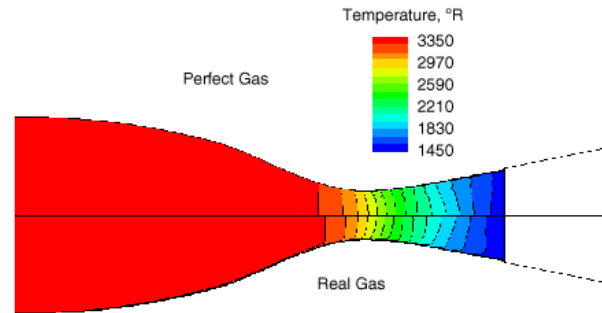


Figure 4. Comparison of Temperature for Perfect and Real Gas Models

Centerline pressure at the exit of this zone was 794 psi for perfect gas and 689 psi for the real gas, while temperature at the same point was 1493°R for perfect gas and 1450°R for real gas. Thus the real gas appears to be expanding more than the perfect gas.

The largest difference between the two cases in the subsonic section is in density, because the pressure and temperature are being set. Figure 5 compares the density between the two gas models, and it is seen that the real gas density (0.43 slugs/ft³) is much less than the perfect gas density (0.49 slugs/ft³). At the zonal exit these values are 0.038 slugs/ft³ and 0.043 slugs/ft³ for the real and perfect gases, respectively.

The reason for the large density difference is explained by Fig. 6, which shows the compressibility for the real gas model (the perfect gas compressibility is one, by definition). The figure shows an inlet compressibility of 1.283, while at the zone boundary the compressibility was 1.01. Therefore, intermolecular forces made the real gas less compressible, thus indicating repulsive forces between the molecules. At the end of this zone the gas could be closely modeled as a perfect gas since the compressibility is almost one and will remain approximately one in the rest of the supersonic nozzle.

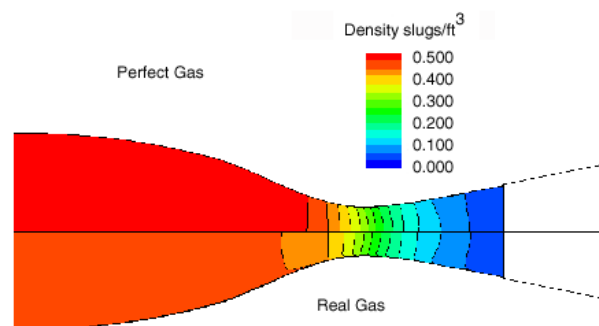


Figure 5. Comparison of Density for Perfect and Real Gas Models

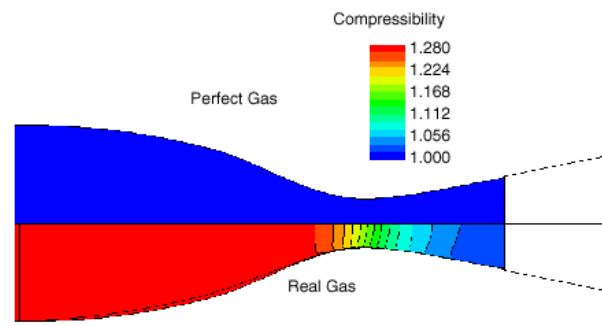


Figure 6. Real Gas Compressibility

The supersonic pressure and temperature are shown in Figs. 7 and 8, respectively, and while the contours appear to vary, the centerline exit values are very close. Pressure equals 0.053 psi and temperature equals 98.75°R for the perfect gas, while pressure equals 0.0509 and temperature equals 98.6°R for the real gas. The velocity (Fig. 9) is somewhat higher for the real gas at the exit (6887 fps), while the perfect gas value is 6619 fps. The exit Mach numbers were noted to be 13.927 and 13.377 for the real gas and the perfect gas, respectively.

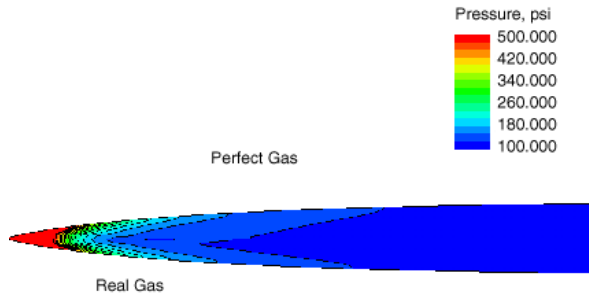


Figure 7. Comparison of Pressure for Perfect and Real Gas Models

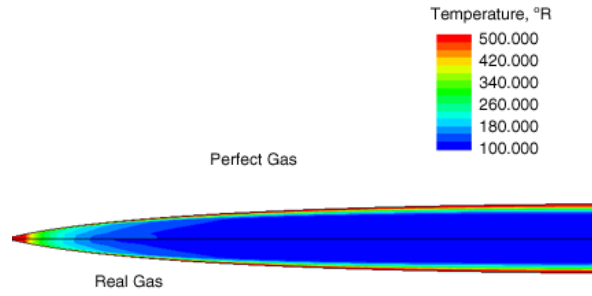


Figure 8. Comparison of Temperature for Perfect and Real Gas Models

The real gas model was compared with test data for this Mach 14 case, and as seen in Fig. 10, the real gas model overpredicted the pitot pressure compared to the data. However, only a single nozzle joint, the most upstream nozzle joint, was modeled out of a total of nine nozzle joints that make up the assembly. The inclusion of the remaining joints could represent a large enough loss to result in accurate agreement.

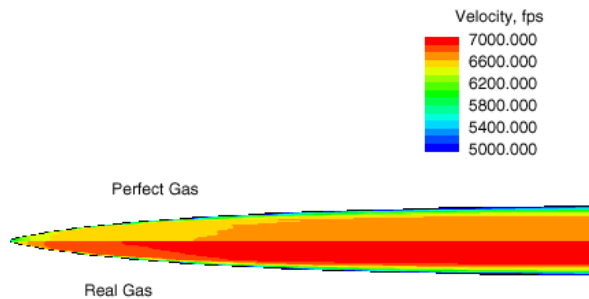


Figure 9. Comparison of Velocity for Perfect and Real Gas Models

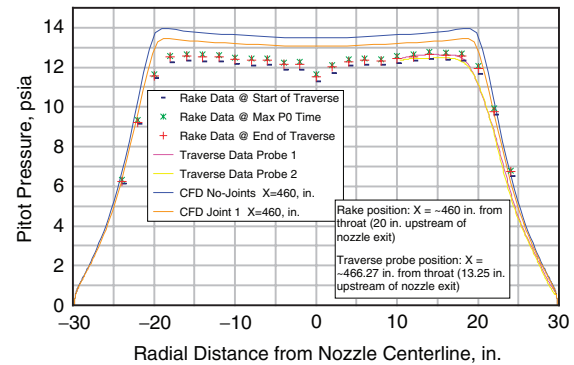
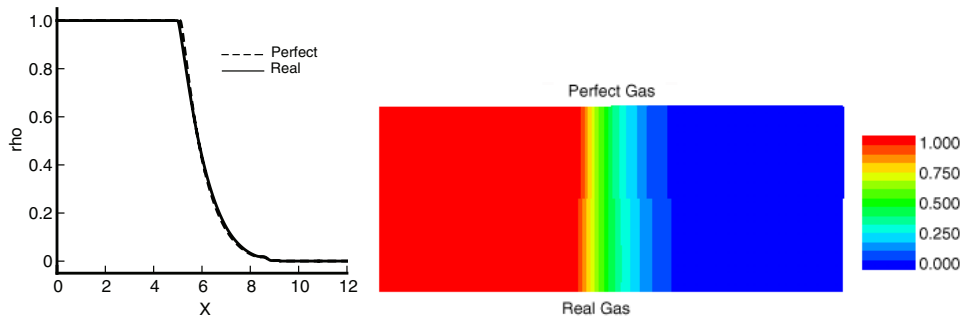


Figure 10. CFD Results for Mach 14, $RE/ft = 3.8E6$

B. High-Pressure Shock Tube

A two-dimensional axisymmetric shock tube demonstration case was undertaken to demonstrate the capability of computing shock tube conditions representative of the AEDC hypervelocity gun facilities. Two sets of chamber total conditions were computed: 1) 20 kpsi and 3600°R, and 2) 100 kpsi and 3600°R, both with hydrogen as the working gas. The low-pressure side of the diaphragm was set at 1 psi and 540°R. The traveling shock was computed for both a perfect gas (calorically imperfect) and a real gas, with the results shown in Figs. 11 through 13. Figure 11 shows a plot of centerline density for a traveling shock starting at 20 kpsi plus a contour plot. It is seen that there is little difference between the gas models for this pressure and hydrogen. In Fig. 11b, the real gas shock can be seen to be traveling slightly faster than the perfect gas shock. For this case the real gas compressibility did not vary substantially from one, as is shown below.



a. Density on Centerline b. Normalized Density Contours
Figure 11. Comparison of Perfect Gas and Real Gas Density for 20-kpsi Shock

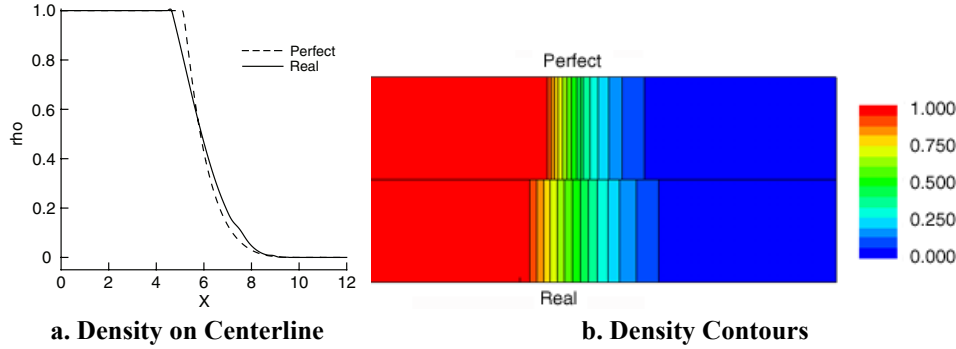


Figure 12. Comparison of Perfect Gas and Real Gas Density for 100-kpsi Shock

The density results for the 100-kpsi traveling shock case are shown in Fig. 12. It can be seen that the perfect gas shock speed is not as fast as the real gas speed. The density variation is as expected from shock theory; however, the pressure ratio (before to after the shock) is so high, 100,000:1, that the details are difficult to see. The density contours show that the interaction region is significantly larger for the real gas than the perfect gas.

Figure 13 compares the real gas compressibility for the two high-pressure cases computed. The compressibility was as high as 1.57 for the 100-kpsi case, while for the 20-kpsi case the maximum was 1.1. This indicates the relative importance of including real gas effects in the two cases, and partially explains why variations for the 20-kpsi case between the real gas and the perfect gas are small, while variations for the 100-kpsi hydrogen are substantial. The variations are also affected by the caloric models.

Because temperature results for the above cases indicated an unexpectedly high temperature in the shock region, a program that solves the one-dimensional ideal shock equations was executed for an additional case with a pressure ratio of 10,000:1. The real gas peak temperature is lower than either the ideal gas or perfect gas. The real gas peak is not as wide as that of the ideal gas or the perfect gas cases, and both the perfect gas and real gas shock speeds appear to be lower than the ideal gas speed. This is consistent with energy being stored as internal energy in the more realistic models, and the results appear to be plausible.

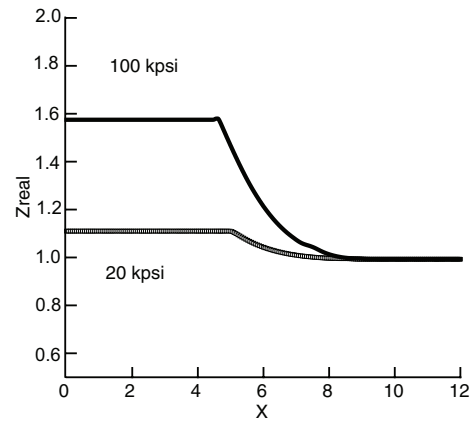


Figure 13. Comparison of Compressibility for 100-kpsi vs 20-kpsi Chamber Pressure

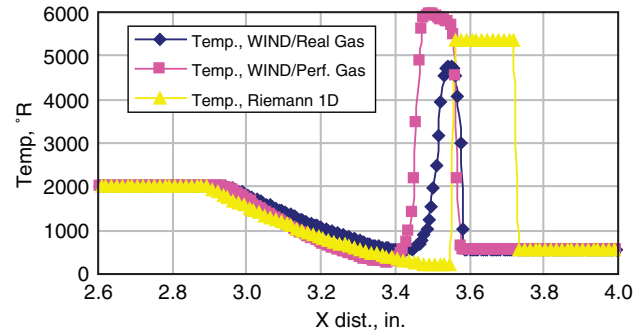


Figure 14. Temperature Comparison of Gas Models for 2-μsec Shock Tube

VII. Summary and Conclusions

Real gas models for nitrogen and hydrogen have been added to the Wind-US program in the structured solver. Real gas modifications have been included only in the Roe flux. However, since the real gas eigenvalues and eigenvectors have been derived, extension to other solvers should be simplified. The real gas model has been developed to allow investigators to add gases arbitrarily by including an appropriate thermodynamic evaluation routine.

Two types of problems have been computed for real gases and compared to perfect gas solutions, i.e., a converging-diverging Mach 14 nozzle and a high-pressure shock tube. The results show that real gas effects can significantly alter flow and thermodynamic parameters as compared to perfect gas results. Comparisons with perfect gas models and nozzle data indicate that reasonable results are being attained. Further validation should be

accomplished to increase confidence in the models, especially since the high-pressure conditions considered are beyond the normal experience of many investigators.

Work is continuing on more complete incorporation of the real gas capability into the Wind-US code, and future plans are to incorporate the models in the unstructured solver as well as the structured solver.

References

- ¹Anderson, John D., Jr., *Hypersonic and High Temperature Gas Dynamics*, McGraw-Hill, 1989, p. 391.
- ²Nelson, C. C. and Power, G. D., "CHSSI Project CFD-7: The NPARC ALLIANCE Flow Simulation System," AIAA-2001-0594, 39th AIAA Aerospace Sciences Meeting and Exhibit, Reno, NV, January 8-11, 2001.
- ³Warming, R. F., Beam, R. M., and Hyatt, B. J., "Diagonalization and Simultaneous Symmetrization of the Gas-Dynamic Matrices," *Mathematics of Computation*, Vol. 29, No. 132, Oct. 1975, pp. 1037-1045.
- ⁴Janus, M. J., "The Development of a Three-Dimensional Split Flux Vector Euler Solver with Dynamic Grid Applications," Master's Thesis, Mississippi State University, August 1984.
- ⁵Li, D., Xia, G., and Merkle, C. L., "Analysis of Real Fluid Flows in Converging Diverging Nozzles," AIAA 2003-4132.
- ⁶Choi, J., Oh, S. and Jeung, I., "Correction of Roe's Approximate Riemann Solver for Real Gas Equation of State," AIAA 2002-3293.
- ⁷Lemmon, E. W., McLinden, M. O., and Friend, D. G. "Thermophysical Properties of Fluid Systems" in *NIST Chemistry WebBook, NIST Standard Reference Database Number 69*, Eds. P.J. Linstrom and W.G. Mallard, National Institute of Standards and Technology, Gaithersburg MD, 20899, March 2003 (<http://webbook.nist.gov>).
- ⁸Reid, R. C., Prausnitz, J. M., and Polling, B. E., *The Properties of Gases and Liquids*, 4th edition, McGraw-Hill, 1986.
- ⁹Span, Roland, *Multiparameter Equations of State: An Accurate Source of Thermodynamic Property Data*, Springer, 2000, ISBN 3-540-67311-3.
- ¹⁰Reynolds, W. C., "Thermodynamic Properties in SI, Graphs, Tables, and Computational Equations for 40 Substances," Stanford University Press, 1979, ISBN 0-917606-05-1.